J. Am. Chem. Soc. **1988**, *110*, 5329–5339

interaction between the proton and one or more chlorine nuclei, the last being 1 order of magnitude less than the other two. Line-shape analysis shows that the dipolar splitting between the proton pair is 8.6 ± 0.5 kHz at 220 MHz, yielding a shift anisotropy δ of −22.7 ppm. The proton shielding parameters were further confirmed by homonuclear decoupling. Both the interproton distances, 2.5 ± 0.2 Å, and the orientation of this dipolar interaction with respect to the shift tensor that can be deduced from the data are in good accord with the structure of $ZrClO_xH_y$. Simple line-shape analysis of the heteronuclear dipolar interaction from the MAS rotation sideband shows that the proton pairs are also coupled to one or more equivalent chlorine nuclei with a $\bar{d}(H-Cl) \sim 2.7$ Å, consistent with the known structure of $ZrClO_xH_y$.

Acknowledgment. The NMR part of this research was supported by the U.S. Department of Energy, Office of Basic Energy Sciences, Chemical Sciences Division, under Contract W-7405-Eng.82. The synthetic and structural portion (R.P.Z.) was supported by the National Science Foundation, Solid State Chemistry (Grant DMR-8318616), and was also performed in the facilities of the Ames Laboratory, DOE.

Spectroscopic Studies on Ferrous Non-Heme Iron Active Sites: Magnetic Circular Dichroism of Mononuclear Fe Sites in Superoxide Dismutase and Lipoxygenase

James W. Whittaker[†] and Edward I. Solomon*

Contribution from the Department of Chemistry, Stanford University,
Stanford, California 94305. *Received July 31, 1987*

Abstract: The geometric and electronic structures of ferrous active sites in Fe superoxide dismutase (FeSD) and soybean lipoxygenase (SBL) have been probed by a combination of optical absorption, circular dichroism, and magnetic circular dichroism spectroscopies in the near-IR spectral region. Distinct ligand field excited state spectra have been observed for the two ferrous proteins, indicating significant differences in active site structures. Temperature and magnetic field dependent MCD intensity for the excited state spectral features have been used to obtain detailed information on the EPR inaccessible ground states in the ferrous complexes. Analysis of the MCD data has provided estimates of ground-state splitting parameters on the two proteins and two ferrous model complexes; the origin of the unusual field dependence of the MCD intensity at saturation has been explained in terms of Zeeman mixing within a $M_S = \pm 2$ non-Kramers doublet which is rhombically split. It is determined that a spin Hamiltonian is not an appropriate description for high-spin ferrous ground-state zero-field splittings for a distorted octahedral or square-pyramidal site. An alternative calculation which includes significant orbital contributions to the ground-state splittings gives the rhombic and Zeeman splittings of the lowest doublet of a ferrous site in terms of spin–orbit coupling within the ligand field split t_{2g} orbitals. This permits quantitative estimates of the t_{2g} d orbital splittings from the MCD intensity data. The ground- and excited-state d orbital splittings have been interpreted in terms of geometric and electronic structures for the active site ferrous complexes: for FeSD, a five-coordinate structure and an effective distorted square pyramidal electronic symmetry is indicated by the experimental data, while for SBL a rhombically distorted roughly octahedral six-coordinate structure is determined. Development of ground- and excited-state probes of the ferrous environments in the enzyme active sites has allowed the interaction of the ferrous sites with small molecules to be studied spectroscopically. The ferrous sites in these two proteins appear to be inaccessible to exogenous ligands, which is significant with respect to their O_2 reactivity in catalysis.

Non-heme Fe centers have been identified as the catalytic active sites in a large number of enzymes whose mechanisms involve interactions of dioxygen with a ferrous site.[1] Typically both ferric and ferrous oxidation states are accessible in these systems, in which the native enzyme may stabilize the ferrous oxidation state. These non-heme Fe proteins may be characterized by the number of interacting iron centers in the active site. Mononuclear Fe sites contain a single metal ion coordinated to the protein. This type of active site is observed in the enzymes Fe superoxide dismutase (FeSD),[2] soybean lipoxygenase (SBL),[3] phenylalanine hydroxylase (PAH),[4] catechol 2,3-dioxygenase (2,3-CTD), etc.[5] These enzymes respectively catalyze the dismutation of superoxide, hydroperoxidation of unsaturated lipids, aromatic ring hydroxylation, and catechol ring cleavage. A second class of non-heme Fe active sites contains a bridged binuclear Fe complex and is found for example in the oxygen carrier protein hemerythrin, where dioxygen reversibly binds to the binuclear ferrous unit, forming a binuclear ferric peroxide complex.[6]

Detailed structural studies are emerging for representative Fe sites of both mono and binuclear types. Crystal structures of the native ferric active site of FeSD from *Ps. ovalis*[7] and *E. coli*[8] have been reported, including one anion complex. These structures are currently at 3 Å resolution and are awaiting completion of the protein sequence for refinement. Various interpretations of the electron density map at the current resolution have been presented; most recently a five-coordinate trigonal-bipyramidal site structure has been proposed for the *E. coli* Fe site.[9] A crystal structure

---

[†] Present address: Department of Chemistry, Carnegie Mellon University, Pittsburgh, PA 15213.

(1) Hayaishi, O.; Nozaki, M.; Abbott, M. In *The Enzymes*, 3rd ed.; Boyer, P. D., Ed.; Academic: New York, 1970.

(2) Slykehouse, T. O.; Fee, J. A. *J. Biol. Chem.* **1976**, *251*, 5472–5477.

(3) Veldink, G. A.; Vliegenthart, J. F. G.; Boldingh, J. *Prog. Chem. Fats Other Lipids* **1977**, *15*, 131–161.

(4) Gottschall, D. W.; Dietrich, R. F.; Benkovic, S. J.; Shiman, R. *J. Biol. Chem.* **1982**, *257*, 845–849.

(5) Nozaki, M.; Kagamiyama, H.; Hayaishi, O. *Biochem. Z.* **1963**, *338*, 582–590.

(6) (a) Okamura, M. Y.; Klotz, I. M. In *Inorganic Biochemistry*; Eichorn, G. L., Ed.; Elsevier: Amsterdam, 1973; pp 320–343. (b) Kurtz, D. M., Jr.; Shriver, D. F.; Klotz, I. M. *Coord. Chem. Rev.* **1977**, *24*, 145–178.

(7) Ringe, D.; Petsko, G. A.; Yamakura, F.; Suzuki, K.; Ohmori, D. *Proc. Natl. Acad. Sci. U.S.A.* **1983**, *80*, 3879–3883.

(8) Stallings, W. C.; Powers, T. B.; Pattridge, K. A.; Fee, J. A.; Ludwig, M. L. *Proc. Natl. Acad. Sci. U.S.A.* **1983**, *80*, 3884–3888.

(9) Stallings, W. C.; Pattridge, K. A.; Ludwig, M. L. In *Superoxide and Superoxide Dismutase in Chemistry, Biology, and Medicine*; Rotilio, G., Ed.; Elsevier: New York, 1986.

0002-7863/88/1510-5329$01.50/0 © 1988 American Chemical Society

exists for the binuclear ferric site in hemerythrin providing basic geometric structural information for the iron coordination: one being six coordinate perturbed octahedral and the second either five-coordinate distorted trigonal bipyramidal or six-coordinate depending on anion.[10]

The chemistry of the mononuclear non-heme Fe enzymes FeSD and SBL has been particularly well characterized through kinetic analysis[11-14] and labeling studies[16,17] which have provided insight into the catalytic mechanisms of these enzymes. For FeSD, the native ferric site appears to be reduced by 1 equiv of superoxide in a step that is inhibited by anion (N_3^-) coordination to the metal center and in which dioxygen is produced; in a second step, a second equivalent of superoxide is reduced by the ferrous site to form hydrogen peroxide.[17] This second step appears to be insensitive to N_3^- but is inhibited at high concentrations of the noncoordinating perchlorate anion.[18] The mononuclear Fe site in SBL, which is ferrous in the native enzyme, requires oxidation to the ferric oxidation state for catalysis.[19-21] Transient kinetic studies of the reaction of this yellow ferric enzyme with its unsaturated lipid substrate indicate that the Fe site is probably rapidly reduced under turnover conditions[14] and that a ferrous species is likely to be directly involved in oxygen interactions leading to the formation of peroxide products. The key mechanistic role of the ferrous oxidation state in the reactivity of each of these active sites indicates the importance of spectroscopic probes that can be used to develop detailed insight into the structures of the ferrous sites in these enzymes and their interaction with exogenous ligands.

The ferric non-heme iron active sites have been spectroscopically and crystallographically most extensively studied. These complexes are easily accessible spectroscopically because the $S = {}^5/_2$ ground state is EPR active,[2,21] and the easily reduced ferric center is associated with intense low-energy ligand-to-metal charge-transfer absorption in the visible–near-UV spectral region.[2,22,23] In contrast, the ferrous active sites are generally considered to be spectroscopically inaccessible. The charge transfer absorption features of the ferric sites disappear on reduction, and the even electron (d^6) ferrous site which is high spin with $S = 2$ is EPR inaccessible as a result of large zero field splittings of the 5-fold degenerate non-Kramers ground state. However, due to its open shell electronic structure, there are a number of ligand field excited states for ferrous iron leading to a number of spin allowed d → d transitions which are very sensitive probes of geometry. We have been developing a combination of optical absorption, CD, and MCD spectroscopies in the near-IR spectral region as probes of the ferrous active sites.[24,25] This combination of spectroscopies, each of which is governed by different selection rules, has proven particularly effective, allowing observation of d → d excited state spectral features; in addition, temperature and field dependent MCD of these d → d transitions provides information relating to the ground state of these paramagnetic ferrous centers. These Fe^{2+} ground- and excited-state spectral features combined with appropriate ligand field analysis provide detailed insight into the geometry and exogenous ligand binding properties of the enzyme active sites and allow a correlation of active site properties over enzymes involved in different aspects of ferrous–oxygen reactivity.

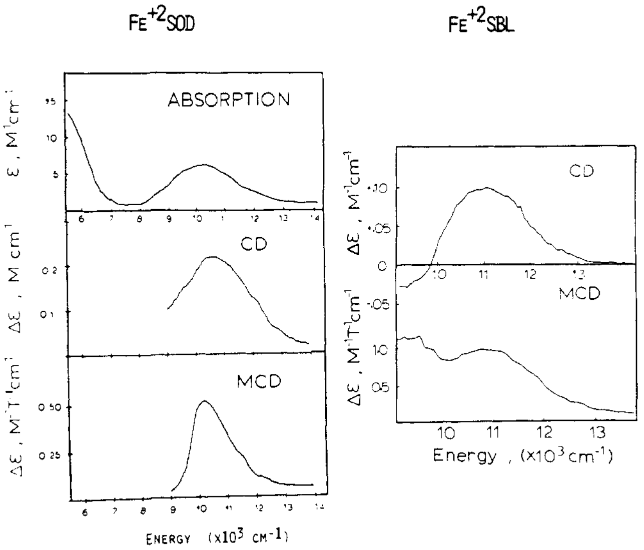

Figure 1. Ligand field spectra for the non-heme Fe^{2+} sites in SD and SBL. (Left) Optical absorption, CD, and MCD spectra for ferrous SD, 3–7 mM in Fe, in 50 mM K_2HPO_4 buffer, pH 7.4. (Right) CD and MCD spectra for native lipoxygenase, 1–2 mM in Fe, in 50 mM Na borate pH 9.0. The MCD samples were prepared in 50% glycerol solution and spectra were recorded at 4.2 K in a 3 mm path length cell.

Experimental Section

FeSD was isolated from *E. coli B* cell paste (ATCC 11303) according to published procedures.[2] SBL was purified from soybeans (Williams variety Lot No. 3070, Tabor Seed Division, Decatur, IL) according to a modification of the published procedure,[26] which involved replacement of ultrafiltration steps by ammonium sulfate precipitation and final chromatography of the enzyme on phenylsepharose CL-4B in an adaptation of a previously reported procedure.[27] This provided enzyme substantially free from the heme contaminants which interfere in MCD experiments. The FeSD and peroxidase-free SBL prepared in this way had nearly maximal specific activity and were homogeneous by SDS-PAGE. Metal content for both FeSD and SBL was determined by atomic absorption analysis with use of a Perkin-Elmer Model 2380 graphite furnace atomic absorption spectrometer. The ferrous complexes of 1,4,8,11-tetramethyl-1,4,8,11-tetraazacyclotetradecane (tetramethylcylam, TMC) [Fe(TMC)X], X = Br^-, N_3^-, NC–CH_3, were prepared according to published procedures.[28]

Optical absorption spectra were typically recorded on a Cary 17 spectrometer; CD spectra were recorded on a Jasco J-500 spectropolarimeter with a red-sensitive S-1 phototube permitting data collection to 1100 nm. Modification of the Jasco J-500 for near-IR MCD spectral studies with an Oxford Instruments SM-4 superconducting magnet capable of 1.7 K and 6.0 T operation has been reported elsewhere.[29] Optical glasses for low-temperature MCD studies were prepared by dialysis of enzymes versus buffer containing 50% glycerol. The concentrated samples (1–5 mM in Fe) were injected into a cell constructed by

---

(10) Stenkamp, R. E.; Sieker, L. C.; Jensen, L. H. *J. Am. Chem. Soc.* **1984**, *106*, 618–622.

(11) Bull, C.; Fee, J. A. *J. Am. Chem. Soc.* **1985**, *107*, 3295–3304.

(12) Egmond, M. R.; Brunori, M.; Fasella, P. M. *Eur. J. Biochem.* **1976**, *61*, 93–100.

(13) Cook, H. W.; Lands, W. E. M. *Can. J. Biochem.* **1975**, *53*, 1220–1231.

(14) Egmond, M. R.; Fasella, P. M.; Veldink, G. A.; Vliegenthart, J. F. G.; Boldingh, J. *Eur. J. Biochem.* **1977**, *76*, 469–479.

(15) Hamberg, M.; Samuelsson, B. *J. Biol. Chem.* **1967**, *242*, 5329–5335.

(16) Egmond, M. R.; Vliegenthart, J. F. G.; Boldingh, J. *Biochem. Biophys. Res. Commun.* **1972**, *48*, 1055–1060.

(17) Fee, J. A.; McClune, G. J.; Lees, A. C.; Zidovetski, R.; Pecht, I. *Isr. J. Chem.* **1981**, *21*, 54–58.

(18) Fee, J. A.; McClune, G. J. In *Mechanisms of Oxidizing Enzymes*; Singer, T. P., Ondaza, R. N., Eds.; Elsevier/North Holland: Amsterdam, 1978; pp 273–284.

(19) Slappendel, S.; Malstrom, B. G.; Peterson, L.; Ehrenberg, A.; Veldink, G. A.; Vliegenthart, J. F. G. *Biochem. Biophys. Res. Commun.* **1982**, *108*, 673–677.

(20) Cheesbrough, T. M.; Axelrod, B. *Biochemistry* **1983**, *22*, 3837–3840.

(21) de Groot, J. J. M. C.; Veldink, G. A.; Vliegenthart, J. F. G.; Boldingh, J.; Wever, R.; van Gelder, B. F. *Biochim. Biophys. Acta* **1975**, *377*, 71–79.

(22) de Groot, J. J. M. C.; Garssen, G. A.; Veldink, J. F. G.; Vliegenthart, J. F. G.; Boldingh, J.; Egmond, M. R. *FEBS Lett.* **1975**, *56*, 50–54.

(23) Spaapen, L. J. M.; Veldink, G. A.; Liefkens, T. J.; Vliegenthart, J. F. G.; Kay, C. M. *Biochim. Biophys. Acta* **1979**, *574*, 301–311.

(24) Whittaker, J. W.; Solomon, E. I. *J. Am. Chem. Soc.* **1986**, *108*, 835–836.

(25) Reem, R. C.; Solomon, E. I. *J. Am. Chem. Soc.* **1987**, *109*, 1216–1226.

(26) Finazzi-Agro, A.; Avigliano, L.; Veldink, G. A.; Vliegenthart, J. F. G.; Boldingh, J. *Biochim. Biophys. Acta* **1973**, *326*, 462–470.

(27) Flurkey, W. H.; Young, L. W.; Jen, J. J. *J. Agric. Food Chem.* **1976**, *26*, 1474–1476.

(28) Hodges, K. D.; Wollmann, R. G.; Barefield, E. K.; Hendrickson, D. N. *Inorg. Chem.* **1977**, *16*, 2746–2751.

(29) Spira-Solomon, D. J.; Allendorf, M. A.; Solomon, E. I. *J. Am. Chem. Soc.* **1986**, *108*, 5318.

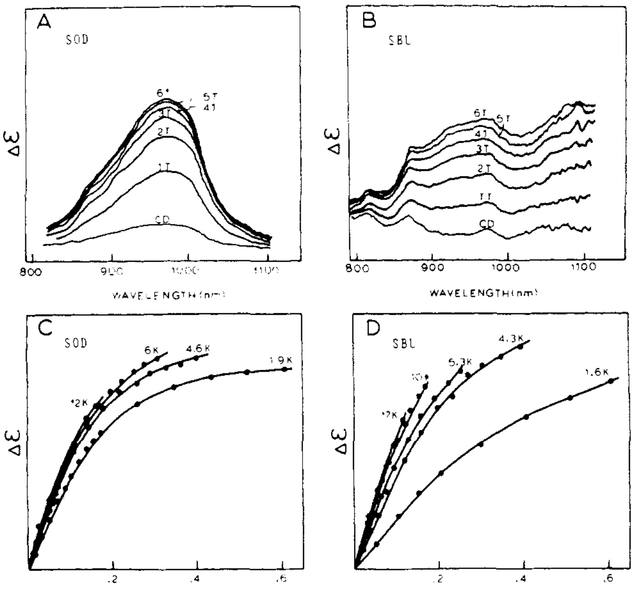

Figure 2. Saturation of MCD for non-heme ferrous active sites. The field dependence of MCD signal intensity for FeSD (*A*, λ = 950 nm) and SBL (*B*, λ = 900 nm) indicating approach to a saturation limit intensity at 4.2 K. The signal amplitude for a range of field strengths from 0.1 to 6.0 T and temperatures from 1.6 to 12 K is plotted as saturation magnetization curves for FeSD (C) and SBL (D).

sandwiching two quartz disks with a rubber gasket and frozen slowly during insertion into the cryostat to reduce strain. Depolarization of the frozen samples was checked by measuring the CD of a Ni tartarate solution placed alternately before and after the sample in the optic path.[30] Samples exhibiting depolarization due to strain birefringence were thawed and refrozen. Near-IR absorption spectra of ferrous FeSD were obtained by lyophilizing the protein and redissolving in D_2O. Matched sample and reference solutions were prepared, and the sample was reduced by anaerobic addition of $Na_2S_2O_4$; the reference solution effectively blanked absorption due to protein vibrational overtone and solvent absorption in the region 1000–1800 nm.

Results

A. Spectra. Spectroscopically distinct Fe sites are observed in ferrous FeSD and SBL (Figure 1). For FeSD, a single broad feature centered near 10 500 cm^{-1} is observed in absorption, CD, and MCD spectra. A line width change that is observed in the MCD of this feature appears to relate to the glycerol which is used as a glassing agent in these experiments. There is, however, no evidence of direct interactions between the glycerol and the iron active site. In ferric FeSD, glycerol glassing agent leads to an approximately 50% sharpening of EPR spectral features without any observable shift in *g* values, and the ferric site titrates normally with anions in the presence of glycerol.[31] Absorption measurements extending to lower energy reveal a second d → d transition below 6000 cm^{-1} which appears to be peaking in the vicinity of 5000 cm^{-1} with an extinction $\epsilon \sim 15\ M^{-1}\ cm^{-1}$.

For SBL, two features are resolved in the near-IR at approximately 10 000 cm^{-1} split by 1500 cm^{-1}; the resolution of these two features is particularly clear in the CD spectra where the rotational strengths of the two bands have opposite signs. No absorption data are reported for SBL because of interference from scattering in the slightly turbid solutions of highly concentrated enzyme required to observe extremely weak d → d spectra. Under our conditions, absorption bands with $\epsilon > 1\ M^{-1}\ cm^{-1}$ should have been observable which places an upper limit on the absorption intensity of the bands at 9 300 and 10 900 cm^{-1}.

B. Saturation Magnetization. The MCD signal for both SBL and FeSD is found to increase at low temperature, indicating C-term behavior[32,33] consistent with the paramagnetic ground state of high-spin ferrous iron. As shown in Figure 2A,B at the lowest temperature, the MCD intensity is observed to saturate with increasing magnetic field for both FeSD and SBL, indicating population of only one component of a Zeeman split paramagnetic ground state.[34] Saturation curves as in Figure 2C,D obtained at increasing temperatures when plotted as a function of the reduced parameter $\beta H/2kT$ are not found to superimpose, but instead are nested, a behavior observed for other metal sites with $S > {}^1/_2$ and associated with zero field splitting of the ground state.[35,36]

C. Model Complexes. In order to calibrate the results obtained for the ferrous active sites in the two enzymes, structurally defined models for which some magnetic characterization of the ground states has been reported were studied in parallel experiments. [Fe(TMC)Br]Br (TMC: 1,4,8,11-tetramethyl-1,4,8,11-tetraazacyclotetradecane; tetramethylcyclam) was selected as a model for five-coordinate ferrous iron. Although a crystal structure is not available for this complex, analogy with the corresponding nickel complex for which the geometry has been crystallographically defined has been used to assign a five-coordinate, square-pyramidal ($\sim C_{4v}$) geometry to the ferrous site.[28] We observe a single absorption feature at 10 500 cm^{-1}, consistent with the proposed structure (vide infra). Susceptibility data for this complex has been interpreted in the spin Hamiltonian formalism in terms of an axial zero field splitting of the ground state with $D = 5.7\ cm^{-1}$.[28] Octahedral coordination of ferrous iron in the Tutton salt $Fe(NH_4)_2(SO_4)_2{\cdot}6H_2O$ has been crystallographically defined[37] and extensive studies of the paramagnetism of this complex have been reported,[38] including single-crystal susceptibility data.[38c] The magnetochemistry of this complex has been interpreted in terms of a strong rhombic distortion in a ground state exhibiting a large negative zero field splitting, $D = -21\ cm^{-1}$.[38b] Absorption data on this complex[39] show a pair of absorption features near 10 000 cm^{-1} split by approximately 2500 cm^{-1}.

Low-temperature MCD spectra of these ferrous model complexes either in Nujol mulls or in ethanol–glycerol glasses exhibit C-terms in the near-IR. For [Fe(TMC)Br]Br a single C-term is observed at 10 500 cm^{-1}; broad C-terms are observed for ferrous Tutton salt near 10 000 cm^{-1}. The saturation of the MCD signal for [Fe(TMC)Br]Br is shown in Figure 3A and more complete saturation magnetization data for these two model complexes are plotted in Figure 3B,C. The saturation magnetization of these model complexes again exhibits the nested curves characteristic of a zero field split paramagnetic ground state.

D. Ligand Binding. The sensitivity of the excited-state spectra and the associated MCD saturation magnetization curves to coordination environment and zero field splitting of the ferrous ground state make these valuable probes of ligand interactions at the ferrous sites. However, as presented in Figure 4, the MCD spectra and saturation magnetization for both FeSD and SBL are unchanged in the presence of 0.5 M KN_3 and high concentrations of NaF or NaOCN. The spectral changes resulting from the chemical perturbation of a ligand substitution have thus been calibrated by examining a set of model complexes. Variation of the apical ligand in the series [Fe(TMC)X] (X = Br^-, N_3^-, and $NC{-}CH_3$) has been described, and these complexes are reported to retain a square-pyramidal geometry.[28] In contrast to the protein sites, systematic variation in the apical ligand over the model complex series results in a significant increase in energy of the

---

(30) Browett, W. R.; Fucaloro, A. F.; Morgan, T. V.; Stephens, P. J. *J. Am. Chem. Soc.* **1983**, *105*, 1868–1872.

(31) Whittaker, J. W.; Solomon, E. I., unpublished results.

(32) Stephens, P. J. *J. Chem. Phys.* **1970**, *52*, 3489.

(33) Piepho, S. B.; Schatz, P. N. *Group Theory in Spectroscopy with Applications to Magnetic Circular Dichroism*; John Wiley: New York, 1984.

(34) Schatz, P. N.; Mowery, R. L.; Krauz, E. R. *Mol. Phys.* **1978**, *35*, 1537–1557.

(35) Thomson, A. J.; Johnson, M. K. *Biochem. J.* **1980**, *191*, 411–420.

(36) Johnson, M. K.; Robinson, A. E.; Thomson, A. J. In *Iron Sulfur Proteins*; Spiro, T. G., Ed.; Wiley: New York, 1979; pp 367–406.

(37) (a) Hofmann, W. *Z. Krist.* **1931**, *78*, 278. (b) Montgomery, H.; Lingafelter, E. C. *Acta Crystallogr.* **1964**, *17*, 1479.

(38) (a) Richardson, J. T.; Sapp, R. C. *J. Chem. Phys.* **1958**, *29*, 337–339. (b) Sapp, R. C. *J. Chem. Phys.* **1959**, *30*, 326–327. (c) Ohtsuka, T.; Abe, H.; Kanda, E. *Sendai Tohoku University, Science Reports* **1957**, *9A*, 476–491.

(39) Holmes, O. G.; McClure, D. S. *J. Chem. Phys.* **1957**, *26*, 1686.

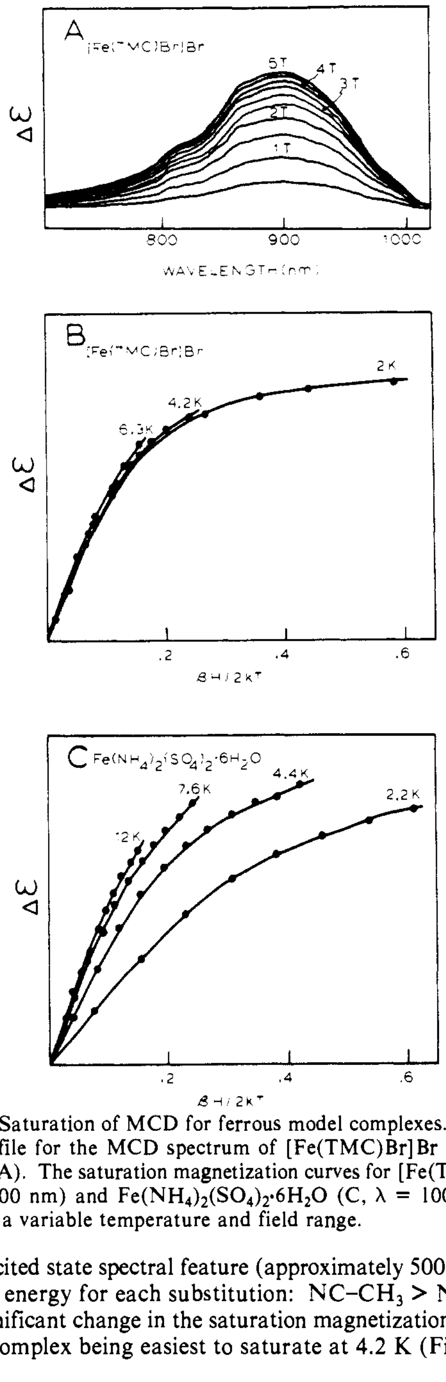

Figure 3. Saturation of MCD for ferrous model complexes. The saturation profile for the MCD spectrum of [Fe(TMC)Br]Br at 4.2 K is shown in (A). The saturation magnetization curves for [Fe(TMC)Br]Br (B, λ = 900 nm) and $Fe(NH_4)_2(SO_4)_2{\cdot}6H_2O$ (C, λ = 1000 nm) are shown for a variable temperature and field range.

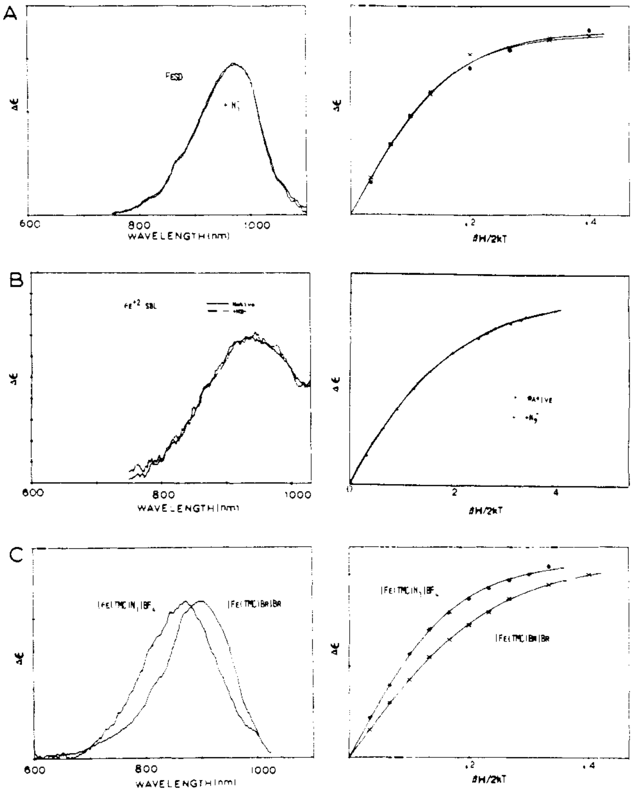

Figure 4. Ligand interactions. Low-temperature MCD spectra (left) and saturation magnetization curves (right) for FeSD (A), SBL (B), and the square-pyramidal model complexes [Fe(TMC)Br]Br and [Fe(TMC)N_3]BF_4 (C). Protein samples were prepared in 50% glycerol buffer solutions as described in the legend to Figure 1; these samples were made 0.5 M in KN_3 for the ligand binding study. Model complexes were prepared in 50% glycerol/ethanol glassing solvent. Spectra and saturation data were obtained at 4.2 K.

d → d excited state spectral feature (approximately 500-cm^{-1} shift to higher energy for each substitution: NC–CH_3 > N_3^- > Br^-) and a significant change in the saturation magnetization behavior, the N_3^- complex being easiest to saturate at 4.2 K (Figure 4C).

Analysis

A. d → d Transitions: Ligand Field Theory. The spin allowed ligand field spectra for ferrous complexes can be relatively simply interpreted in terms of one-electron orbital diagrams as the ground configuration corresponds to one electron added to a half-filled 3d subshell.[40,41] For octahedral coordination the ligand field splitting (Figure 5A) between the $^5T_2$ ground state and the ^5E excited state is 10Dq, which for O, N, and halide-type ligands is in the range of 10 000 cm^{-1}, leading to prediction of a d → d (t_{2g} → e_g) absorption feature near 1 μm in the near-IR spectral region. Tetragonal distortion of the octahedral complex introduces a weak axial component to the ligand field leading to a small splitting of the ^5E excited state (~1000 cm^{-1}). Removing one axial ligand entirely results in a larger axial perturbation, and in the five-coordinate square-pyramidal complex the splitting in the ^5E excited state is much larger, on the order of 5000 cm^{-1}. This C_{4v} type perturbation also leads to a splitting of the orbital degeneracy of the $^5T_{2g}$ ground state, which is more weakly coupled to the ligand field and thus is predicted to have a smaller splitting, on the order of 1000 cm^{-1}, which leaves an orbital doublet, ^5E, lowest (vide infra). Experimentally, the highest energy spin allowed d → d transition for a series of square-pyramidal ferrous complexes is observed at energies greater than 10 000 cm^{-1}. Distortion of the square pyramid along either a C_{2v} or a C_s coordinate leads to a rhombic splitting of the ^5E, and eventually results in a trigonal-bipyramidal (D_{3h}) limiting geometry. The orbital splittings in this D_{3h} case would again result in an orbitally nondegenerate state near 10 000 cm^{-1} and an orbital doublet ground state, but experimentally this situation is distinguished from square-pyramidal coordination by the energy of the highest spin allowed d → d feature, which is experimentally found to be below 10 000 cm^{-1} for trigonal-bipyramidal coordination and oxygen, nitrogen, or halide ligand sets.

Removal of both trans ligands in an octahedral complex leads to square planar four coordination as is represented in the structure of the layered silicate gillespite ($BaFeSi_4O_{10}$).[42] Experimentally an orbitally nondegenerate ground state is found for this coordination geometry, which has been interpreted in terms of interconfiguration mixing of Fe 4s leading to stabilization of a $^5A_1$ orbital ground state.[43] (Figure 5B). The ligand field spectrum of the square-planar ferrous complex is distinguished by unusually high energy spin allowed d → d spectral feature at ~20 000 cm^{-1} in the visible region.[43] Displacing the trans ligands alternately above and below the plane of a square-planar complex leads to tetrahedral coordination. In this limit, there is one spin allowed

---

(40) (a) Ballhausen, C. J. *Introduction to Ligand Field Theory*; McGraw-Hill: San Francisco, 1962. (b) Figgis, B. N. *Introduction to Ligand Fields*; Krieger: Melbourne, 1986.

(41) Lever, A. B. P. *Inorganic Electronic Spectroscopy*, 2nd ed.; Elsevier: New York, 1984.

(42) Pabst, A. *Am. Mineral.* **1943**, *28*, 372.

(43) Burns, R. G.; Clark, M. G.; Stone, A. J. *Inorg. Chem.* **1966**, *5*, 1268–1272.

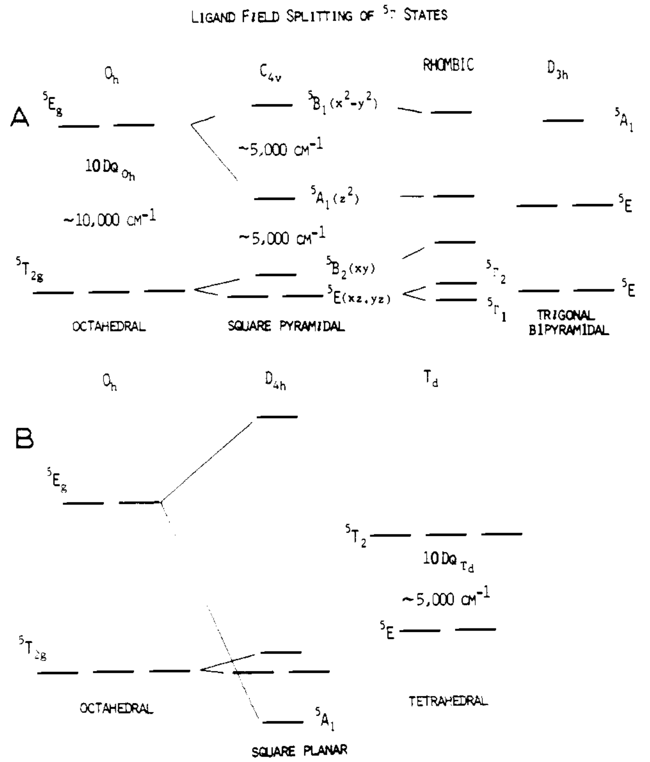

Figure 5. Ligand field splittings correlated over structural distortions of a d^6 metal complex. (A) Removal of one ligand from an octahedral complex leads to correlation of the one electron metal orbital energies over five coordinate square pyramidal and rhombic to trigonal bipyramidal geometry. (B) Correlation over distortions of a four coordinate complex arising from an octahedron by removal of two trans ligands leading to square planar and tetrahedral geometries.

$^5E \rightarrow {}^5T_2$ d → d feature whose energy is defined by the tetrahedral orbital splitting 10 Dq$_{tet}$ ($=-4/9(10\ Dq_{oct})$) ~ 5000 cm^{-1} which places this electronic transition in the IR spectral region.

The correlations between d → d spectra and geometry which are developed through a combination of experiment and ligand field concepts provide a structural probe of ferrous active sites in enzymes. The key information in these spectra is the energies and numbers of ligand field spectral features that can be interpreted in terms of effective site symmetries. For FeSD, the absorption feature above 10 000 cm^{-1} split from the next highest energy d → d feature by about 5000 cm^{-1} effectively defines five coordination and a square-pyramidal limiting geometry for the active ferrous site in this enzyme. This represents the effective electronic symmetry for the ferrous complex and does not rule out distortion along a coordinate leading toward trigonal-bipyramidal geometry. Experimentally, the observed energies and splittings define the square-pyramidal geometry as the most appropriate limiting description, based on the range of energies reported for both square-pyramidal[44] and trigonal-bipyramidal[45] model complexes. For SBL, the pair of d → d transitions observed near 1 μm split by ~1500 cm^{-1} define a distorted octahedral effective site symmetry for this non-heme iron active site.[46] Note that the ε's observed for the d → d bands are consistent as they must be an order of magnitude weaker in SBL consistent with close to centrosymmetric nature of the octahedral ligand field.

B. Temperature-Dependent MCD: Saturation Magnetization.[34-36,50] The ground-state splittings in paramagnetic ferrous

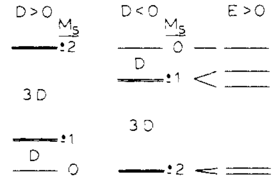

Figure 6. Zero field splitting for a $S = 2$ ground state. The spin Hamiltonian (eq 1) leads to prediction of ground-state splittings characterized by axial (D) and rhombic (E) parameters. A non-Kramers doublet is lowest for $D < 0$; the degeneracy of this doublet is lifted by a lower symmetry distortion as indicated on the right.

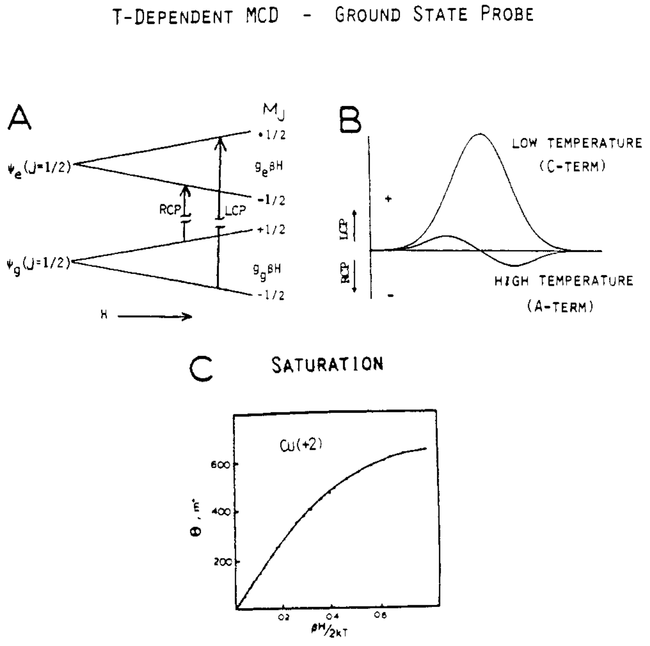

Figure 7. Origin of temperature-dependent effects in MCD spectroscopy. (A) Selection rules for MCD for a transition between Zeeman split paramagnetic ground and excited states. Near cancellation of right- and left-polarized absorption at high temperature leads to a weak A-term MCD signal (B). At low temperature, depopulation of the upper sublevel leads to a large increase in intensity (C-term, B). Saturation of MCD intensity occurs when only the lowest sublevel is populated. The saturation magnetization behavior of an isolated Kramers doublet ground state is equal to $A_{\mathrm{sat\,lim}}$ tanh $(g\beta H/2kT)$ as illustrated in (C) which shows MCD data for a cupric complex recorded over a variable temperature and field range.

complexes provide structural information complementing that available in the excited-state spectra. The splittings within $^5T_{2g}$ are quite sensitive to ligand π interactions rather than the σ interactions which determine the ^5E splitting.[41] Magnetochemical experiments focus on the lowest orbital component of the $^5T_{2g}$ and describe the splitting of its 5-fold spin degeneracy ($S = 2$, $M_S = \pm 2, \pm 1, 0$). This splitting of the lowest component of the $^5T_{2g}$ is usually given in terms of a spin Hamiltonian[47]

$$\mathcal{H} = D(S_z^2 - 1/3S(S+1)) + E(S_x^2 - S_y^2) + g\beta HS \quad (1)$$

where D is the axial and E the rhombic component of the zero field splitting and $g\beta HS$ is the Zeeman splitting which leads to a lifting of the ground state quintet degeneracy as illustrated in Figure 6. In this formalism, a positive value of the zero field splitting parameter D is associated with a nondegenerate $M_S = 0$ sublevel lowest in the ground state, while a negative D value results in an $M_S = \pm 2$ doublet lowest. With rhombic splitting ($|E| > 0$) in the non-Kramers (even electron) ferrous ion, all

---

(44) Riley, D. P.; Merrell, P. H.; Stone, J. A.; Busch, D. H. *Inorg. Chem.* **1975**, *14*, 490.

(45) (a) Ciampolini, M.; Nardi, N. *Inorg. Chem.* **1966**, *5*, 1150. (b) Stoppioni, P.; Mani, F.; Sacconi, L. *Inorg. Chim. Acta* **1974**, *11*, 227. (c) Chia, P. S. K.; Livingstone, S. E. *Aus. J. Chem.* **1969**, *22*, 1613. (d) Mani, F.; Scapacci, G. *Inorg. Chim. Acta* **1980**, *38*, 151. (e) Stoppioni, P.; Morassi, R.; Zanobini, F. *Inorg. Chim. Acta* **1981**, *52*, 101.

(46) Cotton, F. A.; Meyers, M. D. *J. Am. Chem. Soc.* **1960**, *82*, 5023.

(47) Abragam, A.; Bleaney, B. *Electron Paramagnetic Resonance of Transition Ions*; Oxford University Press: London, 1970.

(48) Johnson, K. J. *Numerical Methods in Chemistry*; Marcel Dekker: New York, 1984; pp 312-316.

(49) Bertrand, P.; Guigliarelli, B.; Gayda, J. P. *Arch. Biochem. Biophys.* **1986**, *245*, 305-307.

(50) Bennett, D. E.; Johnson, M. K. *Biochim. Biophys. Acta* **1987**, *911*, 71-80.

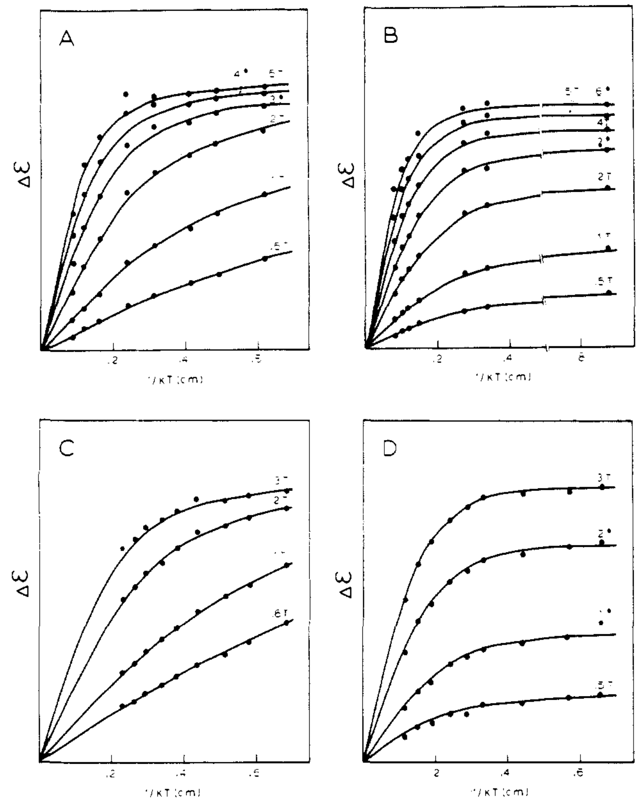

Figure 8. Magnetic field effects on the ground states of FeSD, SBL, and C_{4v} and O_h model complexes. Replot of the saturation data of Figures 2 and 3 in terms of temperature dependence at constant field for FeSD (A), SBL (B), [Fe(TMC)Br]Br (C), and $Fe(NH_4)_2(SO_4)_2{\cdot}6H_2O$ (D). The solid lines are the theoretical profiles obtained by numerically evaluating the orientation averaging integral (eq 6) for the ground-state parameters given in Table I.

ground-state degeneracy will be removed, with observed splittings typically on the order of several cm^{-1} making ferrous complexes inaccessible to EPR spectroscopy. MCD spectroscopy provides in this case an extremely valuable probe of ground-state splittings through the saturation magnetization observed for excited-state spectral features.

MCD intensity in an electronic transition arises from magnetic field interactions in the ground and excited states involved in the transition.[32,33] Figure 7A illustrates the selection rules for circularly polarized absorption ($\Delta M = +1$ for left circular polarization, $\Delta M = -1$ for right circular polarization) which determine the polarization of transitions between the Zeeman split ground and excited states. For transitions between the two states in Figure 7A the transition intensities are equal in magnitude but opposite in sign and have an energy splitting that is small relative to the bandwidth. This leads to a dichroic intensity $\Delta\epsilon_{l-r}$ that at high temperature is observed as a weak derivative-shaped MCD $\mathcal{A}$-term signal (Figure 7B). At low temperature, variation in population over the ground-state sublevels leads to differences in intensity of right and left circular components and an MCD $\mathcal{C}$-term is observed. The temperature and field dependence of the $\mathcal{C}$-term intensity at low temperatures, in the form of saturation magnetization profiles, thus contains information on the ground-state g values. The analysis of saturation magnetization data has been particularly well developed for Kramers degenerate systems.[34-36] The experimental saturation behavior of a typical $S = {}^1/_2$ Cu^{2+} complex is illustrated in Figure 7C, showing that for a Kramers degenerate spin doublet ground state a single saturation magnetization curve results (when plotted as a function of $\beta H/2kT$) over a wide range of variation in both temperature and field.

This is a different behavior than is observed in the Results section for FeSD, SBL (Figure 2), and the ferrous model complexes (Figure 3), where more complex temperature and field dependence leads to a nested set of saturation magnetization curves. For other spin quintet ground state systems this difference has been attributed to thermal population over sublevels that are split in zero field[35,36] as illustrated in Figure 6. Replotting the saturation magnetization data for the two proteins and two model complexes in terms of temperature dependence of MCD intensity at constant field (Figure 8) permits a much clearer separation of field and temperature saturation effects than is possible in the $\beta H/2kT$ presentation (Figures 2 and 3) of saturation magnetization data. For most of the fields at lowest temperature only the lowest sublevel is populated and the presentation in Figure 8 demonstrates that the saturation limit intensity is field dependent for these ferrous complexes requiring a field-induced mixing ($\mathcal{B}$-term) mechanism for the MCD intensity. An unusual feature of these $\mathcal{B}$-terms is the strongly nonlinear magnetic field dependence that is observed, with the intensity converging to a fixed value at high fields for the lowest temperature. This behavior requires that only sublevels within $g\beta$H of the lowest level are involved in this mixing. Thermal population over the ground-state sublevels in FeSD have been studied in a low-field, variable-temperature MCD experiment (Figure 9). Deviations from Curie law behavior occur at both low and high temperature, consistent with a nondegenerate pair of levels lowest in the ground-state split by approximately 2 cm^{-1}, with the next higher level at least 16 cm^{-1} higher in energy. Further, low-temperature saturation curves shown in Figure 8 which relate to population over the lowest two sublevels change progressively in increasing fields in a way that reflects an increase in the splitting, consistent with Zeeman splitting within a ground doublet but not with the alternative level scheme for $D > 0$ (Figure 6). Therefore a doublet of sublevels that can be mixed by a magnetic field is lowest in the ground state, consistent with $D < 0$ in eq 1. While comparable temperature-dependent MCD data are not available for the other complexes, the saturation magnetization data for these are consistent with a similar interpretation. As with FeSD, both the thermal saturation behavior and field dependence of the saturation limit intensity for the C_{4v} model reflect a relatively small splitting of the field-mixed sublevels, while the data for ferrous Tutton salt and SBL are both consistent with a larger splitting.

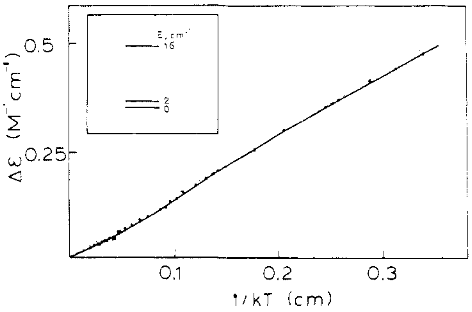

Figure 9. Temperature-dependent MCD for ferrous FeSD at a small sampling field. Data for $H = 0.5$ G, $T = 4.3$–65 K: (---) Curie law behavior for isolated doublet; (—) behavior predicted for splittings indicated in the insert, obtained by a five-parameter fit of the data leaving energies and intensities as independent variables.

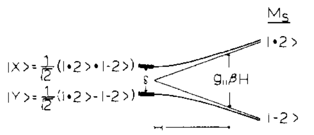

Figure 10. Zeeman interaction for a non-Kramers doublet. The rhombic splitting (δ) leads to real wave functions as given to the left, while sublevel mixing through the Zeeman perturbation leads to pure M_S sublevels.

This field-dependent saturation magnetization behavior can be quantitatively interpreted in terms of a rhombic zero field splitting within the two levels of a non-Kramers $M_S = \pm 2$ (δ, Figure 10). The effective spin Hamiltonian of such an isolated $M_S = \pm 2$ non-Kramers doublet with which we have successfully interpreted the MCD magnetization behavior for these four complexes has a particularly simple form which we have presented in a preliminary report:[24]

$$\mathcal{H} = \begin{array}{c|cc} & |X\rangle & |Y\rangle \\ \hline (X| & +\delta/2 & g_{\parallel}\beta H \cos\theta \\ (Y| & g_{\parallel}\beta H \cos\theta & -\delta/2 \end{array} \tag{2}$$

where X and Y are the real combinations of complex angular momentum wave functions which diagonalize the Hamiltonian of a non-Kramers doublet in zero field. As shown in Figure 10, a rhombic splitting δ within the doublet quenches angular momentum, thus eliminating MCD intensity which requires complex functions. The Zeeman interaction ($g_{\parallel}\beta H \cos\theta$, where θ is the orientation of the magnetic field relative to the zero field splitting axis) represents a purely imaginary perturbation which is off diagonal in a real basis set in eq 2 and mixes these real wave functions, inducing angular momentum and restoring MCD intensity. Diagonalization of this Zeeman mixing leads to complex wave functions associated with pure M_S values (+2, −2) at high fields where $g\beta H \gg \delta$. At intermediate fields, the composition of the lowest sublevel, which determines the saturation limit MCD intensity, is given by

$$|-\rangle = \sin\alpha|+2\rangle - \cos\alpha|-2\rangle \tag{3}$$

where $\alpha = {}^1/_2 \tan^{-1}[\delta/(g_{\parallel}\beta H \cos\theta)]$. Thus from Figure 10 the Zeeman interaction leads to a quadratic splitting of the sublevels through a second-order effect on the energies, while the wave function and hence the saturation limit MCD intensity changes in first order with the field. In the model we are presenting here, the saturation limit MCD intensity, $\Delta\epsilon$, relates to the angular momentum associated with the lowest sublevel that will be proportional to the difference of the squares of the mixing coefficients for the doublet wave function:

$$\Delta\epsilon \propto \cos^2\alpha - \sin^2\alpha = \cos 2\alpha = \cos\theta\Big/\sqrt{(\delta^2/(g_{\parallel}\beta H \cos\theta)^2) + 1} \tag{4}$$

From eq 4, the MCD intensity at saturation is clearly dependent on the magnitude and orientation of the magnetic field.

The temperature dependence of the MCD intensity arises from thermal population over accessible excited sublevels of the ground state, leading to inclusion of Boltzmann factors in the expressions for MCD intensity. The temperature dependence of the MCD intensity at low temperatures thus probes the overall splittings in the ground state resulting from both zero field and Zeeman interactions. The Boltzmann factors for thermal population over non-Kramers doublet sublevels give rise to a hyperbolic tangent temperature dependence involving the factor

$$A(T) = \sqrt{\delta^2 + (g_{\parallel}\beta H \cos\theta)^2}\Big/2kT \tag{5}$$

which includes the rhombic zero field splitting.

In addition to magnitude both eq 4 and 5 depend on the orientation of the magnetic field relative to the zero field splitting axis of the active site. As the MCD studies in Figure 8 are performed on frozen glasses of protein molecules with random orientations, the distribution over orientations must be taken explicitly into account in fitting the MCD data to obtain quantitative ground-state parameters[34,35] (δ and $g_{\parallel}$ in Figure 10). These field dependent energy splitting and interaction terms can be used in a modification of the orientation averaging equation for a Kramers doublet (given in ref 34) to obtain the form of the orientation averaging function for a non-Kramers doublet (eq 6).

$$I = A_{\mathrm{sat\,lim}} \int_0^1 \frac{\cos^2\theta}{\sqrt{\dfrac{\delta^2}{(g_{\parallel}\beta H)^2} + \cos^2\theta}} \times \tanh\left[\frac{\sqrt{\delta^2 + (g_{\parallel}\beta H \cos\theta)^2}}{2kT}\right] \mathrm{d}\cos\theta \tag{6}$$

This equation is appropriate for the anisotropic doublet ($g_{\perp} = 0$) described by the spin Hamiltonian of eq 2 and pure xy polarization for the electronic transition; the effect of relaxing these assumptions is evaluated below. The experimental saturation magnetization data for the two proteins and two model complexes have been analyzed by regression fitting to numerically evaluated eq 6 leaving $A_{\mathrm{sat\,lim}}$, δ, and $g_{\parallel}$ as adjustable parameters. The orientation averaging integral was evaluated by a Simpson's rule procedure[48] and the three parameters were iteratively adjusted until convergence was achieved; the results were tested for uniqueness by choosing initial estimates of the parameters over a wide range.

Table I. Experimental Ground-State Splittings and Ligand Field Parameters

	Fe^{+2}SOD	MODELS		Fe^{+2}SBL
		C_{4V}	O_h	
δ (cm^{-1})	2.9	1.33	8.3	7.24
$g_{//}$	8.78	9.01	8.6	8.20*
$-\Delta$ (cm^{-1})	1200±300	2000±500	250±100	450±100
V/2Δ	0.27±0.05	0.15±0.02	0.3±0.05	0.3±0.05

* Upper limit on $g_{//}$ as d→d transition in SBL contains a significant contribution from Z polarization. (see text)

The calculated fit to the data points is included as the solid lines in Figure 8 and experimental values for δ and $g_{\parallel}$ are presented in the top two rows of Table I. Experimentally, a Zeeman-mixed doublet is lowest in the ground state in each case, suggesting $D < 0$ in spin Hamiltonian terms (eq 1). However, a value of $g_{\parallel}$ exceeding 8.0 is not consistent with $S = 2$ spin Hamiltonian behavior based on a spin only value of $g = 2.00$. Deviations of the electronic g value from 2.00, due to orbital contributions, can of course occur,[49] but it is important to realize that the spin Hamiltonian treatment given in eq 1 is in fact not correct for a high spin ferrous ground state with a doublet set of sublevels lowest in energy (vide infra, section C below).

In a more general treatment, the contribution of z polarization and nonzero $g_{\perp}$ must be considered, since these terms can have significant effects on the MCD saturation behavior.[50] The approach described above has therefore been extended to evaluate the effect of these additional terms on the results obtained in Table I. In order to introduce $g_{\perp}$, the doublet spin Hamiltonian of eq 2, transformed to the complex basis, has been augmented with a perpendicular Zeeman term:

$$\mathcal{H} = \begin{array}{c|cc} & |+\rangle & |-\rangle \\ \hline (+| & {}^1\!/_2(g_{\parallel}\beta H \cos\theta) & {}^1\!/_2(\delta + e^{i\phi}\sin\theta(g_{\perp}\beta H)) \\ (-| & {}^1\!/_2(\delta + e^{-i\phi}\sin\theta(g_{\perp}\beta H)) & -{}^1\!/_2(g_{\parallel}\beta H \cos\theta) \end{array} \tag{7}$$

This doublet Hamiltonian (eq 7) is not readily incorporated into the orientation averaging integrals, and it was therefore evaluated numerically and averaged over angles by a point-by-point summation on a longitude. This adaptation of the C-term intensity equation (eq 10 of ref 34) made it possible to introduce the polarization ratio as an independent parameter in the analysis. With use of this procedure, the saturation magnetization data for the four complexes could be iteratively fit by independent variation of five parameters: δ, $g_{\parallel}$, $g_{\perp}$, xy intensity, and the polarization ratio m_z/m_{xy}. Increasing the number of adjustable parameters from three to five would be expected to improve the quality of the fits relative to the use of eq 6; however, only slight improvements were observed, suggesting that the additional parameters are not strongly required by the data. However, as the polarization ratio was increased beyond about 0.5, the quality of the fits decreased for all complexes except SBL. Within this range of values of the additional parameters, the best fit value of $g_{\parallel}$ obtained from the analysis was consistently greater than 8 for all complexes except SBL as discussed below. The value of $g_{\parallel}$ is thus somewhat dependent on the actual polarization ratio, with the largest value associated with least z polarization. In contrast, the

Table II. Matrix Elements of $\mathcal{H}(^5T_{2g})$ in the $|M_L'M_S\rangle$ Basis

	$\vert 1,2\rangle$	$\vert 1,1\rangle$	$\vert 1,0\rangle$	$\vert 1,-1\rangle$	$\vert 1,-2\rangle$	$\vert 0,2\rangle$	$\vert 0,1\rangle$	$\vert 0,0\rangle$	$\vert 0,-1\rangle$	$\vert 0,-2\rangle$	$\vert -1,2\rangle$	$\vert -1,1\rangle$	$\vert -1,0\rangle$	$\vert -1,-1\rangle$	$\vert -1,-2\rangle$
$\langle 1,2\vert$	$\Delta/3-2\lambda+g\beta H$										$V/2$				
$\langle 1,1\vert$		$\Delta/3-\lambda+\beta H$				$\sqrt{2}\lambda$						$V/2$			
$\langle 1,0\vert$			$\Delta/3-\beta H$				$\sqrt{3}\lambda$						$V/2$		
$\langle 1,-1\vert$				$\Delta/3+\lambda-3\beta H$				$\sqrt{3}\lambda$						$V/2$	
$\langle 1,-2\vert$					$\Delta/3+2\lambda-5\beta H$				$\sqrt{2}\lambda$						$V/2$
$\langle 0,2\vert$		$\sqrt{2}\lambda$				$-2\Delta/3+4\beta H$									
$\langle 0,1\vert$			$\sqrt{3}\lambda$				$-2\Delta/3+2\beta H$				$\sqrt{2}\lambda$				
$\langle 0,0\vert$				$\sqrt{3}\lambda$				$-2\Delta/3$				$\sqrt{3}\lambda$			
$\langle 0,-1\vert$					$\sqrt{2}\lambda$				$-2\Delta/3-2\beta H$				$\sqrt{3}\lambda$		
$\langle 0,-2\vert$										$-2\Delta/3-4\beta H$				$\sqrt{2}\lambda$	
$\langle -1,2\vert$	$V/2$						$\sqrt{2}\lambda$				$\Delta/3+2\lambda+5\beta H$				
$\langle -1,1\vert$		$V/2$						$\sqrt{3}\lambda$				$\Delta/3+\lambda+3\beta H$			
$\langle -1,0\vert$			$V/2$						$\sqrt{3}\lambda$				$\Delta/3+\beta H$		
$\langle -1,-1\vert$				$V/2$						$\sqrt{2}\lambda$				$\Delta/3-\lambda-\beta H$	
$\langle -1,-2\vert$					$V/2$										$\Delta/3-2\lambda-3\beta H$

value of the rhombic splitting parameter δ is virtually unchanged by inclusion of $g_\perp$ and z-intensity terms, indicating that this term is the most reliable parameter arising from this analysis as it depends mainly on the low field temperature dependence of the MCD data. Application of this analysis to the SBL data permits larger values (+ and −) of the polarization ratio and estimates of $g_\parallel$ below 8, with a best fit near $m_z/m_{xy} = 1$ with $g_\parallel = 7.1$ and $\delta = 6.9$ cm^{-1}. In this case, a larger contribution from z polarization appears to lead to a larger variation in $g_\parallel$, while the value of δ is nearly unchanged and the rhombic splitting again appears to be the better defined parameter in this analysis.

It is interesting to note that the highest energy d → d transition of the square-pyramidal model [Fe(TMC)Br]Br, which can be assigned as $^5E \rightarrow {}^5B$ in the C_{4v} point group (Figure 5A), is predicted to be xy polarized under electric dipole selection rules. The highest energy transitions for both the C_{4v} model and for ferrous SD are relatively intense transitions consistent with an electric dipole mechanism, which accounts for the limited z polarization permitted by the MCD saturation data. In contrast, the relatively low intensity of the observed d → d transitions for SBL suggests more vibronic character and thus the possibility of significant z polarization, potentially becoming a problem in our analysis and leading to uncertainty in $g_\parallel$. However, δ is accurately determined independent of m_z/m_{xy} and appears to be the most useful parameter, particularly near the rhombic limit. A more general consideration of the ligand field theory origins of these parameters in the next section shows that δ can be directly interpreted in terms of the $^5T_2$ orbital splittings.

C. Ligand Field Theory of Spin Hamiltonian Parameters. In the spin Hamiltonian for transition-metal complexes, parameters that cause splittings of the ground-state M_S sublevels arise from interactions with orbital excited states through spin–orbit coupling.[51] This is easily pictured for the orbitally nondegenerate ground state which arises from a strong axial distortion of an octahedral complex. This splits the cubic $^5T_{2g}$ ground state in Figure 3 into ^5E and $^5B_2$, where the $^5B_2$ component is lowest as it corresponds to one extra electron in a d_{xy} orbital. The orbitally nondegenerate $^5B_2$ retains the 5-fold degeneracy of the spin quintet, which is not directly split by electrostatic interactions but splits through second-order spin–orbit coupling with the nearby ^5E excited state derived from $^5T_{2g}$ (Figure 11). The magnitude of the zero field splitting D is then given by λ^2/Δ in perturbation theory, where λ is the spin–orbit coupling parameter and Δ is the orbital splitting of the t_{2g} set ($=E_{xz,yz} - E_{xy}$). λ is related to the one-electron spin–orbit coupling parameter ζ by $\lambda = -\zeta/2S$; $\lambda(\mathrm{Fe}^{2+}) = -100$ cm^{-1}, which may be reduced in coordination complexes ~20% through quenching of orbital angular momentum due to covalency. Thus the axial zero field splitting parameter D simply reflects the π ligand field splitting of the t_{2g} orbitals (Δ); the larger the t_{2g} splitting (i.e., the stronger the axial distortion) the smaller the value of D. Note that D is positive for d_{xy} lowest in energy. The rhombic component of the orbital splitting, V, is defined here as the splitting between d_{xz} and d_{yz} orbitals ($=E_{yz} - E_{xz}$).

However, for a weak axial distortion from octahedral symmetry, such as is generally observed in coordination complexes involving weak field axial ligands, tetragonal elongation, or square-pyramidal geometries, the ^5E_g component of the $^5T_{2g}$ state is lowest (Figure 12A), as this corresponds to the extra electron in the xz,yz d orbital set. The key point here is that the ^5E_g ground state has orbital as well as spin degeneracy and the zero field splitting can no longer be described in terms of a spin Hamiltonian. However, for this orbitally degenerate ground state a Hamiltonian may be written which allows for the axial and rhombic t_{2g} orbital splittings, the spin–orbit interactions among all components of the $^5T_{2g}$ state, and the Zeeman interaction within the sublevels of the $^5T_{2g}$ ground state. This is given in eq 8. Here Δ, V, and λ are defined above,

$$\mathcal{H}(^5T_{2g}) = \lambda LS + \Delta(L_z^2 - \tfrac{1}{3}L(L+1)) + V(L_x^2 - L_y^2) + \beta(L_z + 2S_z)H \quad (8)$$

and L operates within an effective $L' = -1$ manifold appropriate for the angular momentum of the cubic T_{2g}. The real t_{2g} d orbitals can be formed from combinations of the $M_{L'} = \pm 1, 0$ complex wave functions which serve as the basis for this calculation: $|1\rangle = d_{xz} - d_{yz}$, $|-1\rangle = d_{xz} + d_{yz}$, $|0\rangle = d_{xy}$. The Zeeman term gives the value of $g_\parallel$ when evaluated within the lowest pair of sublevels of the ground state. The Δ, V convention for orbital splittings within an orbital triplet ground state are adopted from the analysis of spin–orbit coupling in low-spin d^5 which is formally a similar problem.[51] The matrix elements of this Hamiltonian within the $|M_{L'}M_S\rangle$ basis set for $L' = -1$, $S = 2$ are listed in Table II.

A plot of the energy levels arising from this Hamiltonian with no external field is shown in Figure 12B for a range of axial and rhombic distortions. At $\Delta = 0$, spin–orbit coupling leads to multiplets split by 2λ and 3λ having effective $J' = 1$, 2, and 3. The effective $L' = -1$ results in the state of lowest rather than highest J being most stabilized. An axial perturbation which leads to the orbitally degenerate ^5E_g state lowest in energy in the absence

---

(51) Griffith, J. S. *Theory of Transition Metal Ions*; Cambridge University Press: Cambridge, 1964; pp 355–360.

(52) Griffith, J. S. *Proc. R. Soc. London* **1956**, *A235*, 23–36.

(53) Fee, J. A.; Ward, R. L. *Biochem. Biophys. Res. Commun.* **1976**, *71*, 427–437.

(54) Yamakura, F.; Suzuki, K. *Biochim. Biophys. Acta* **1986**, *874*, 23–29.

(55) Beyer, W. F., Jr.; Fridovich, I. *Biochemistry* **1987**, *26*, 1251–1257.

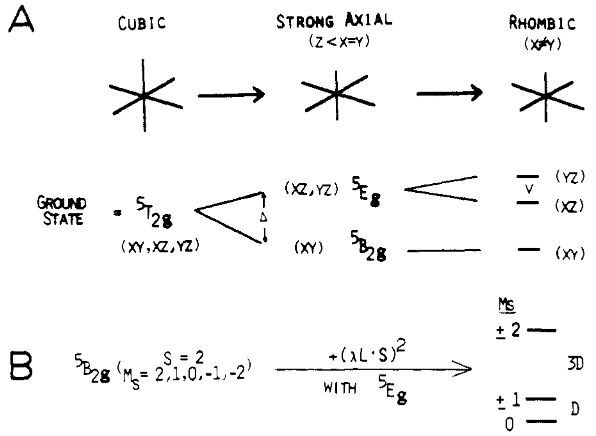

Figure 11. Ligand field theory of spin Hamiltonian parameters. (A) Geometric distortions on a ferrous complex from octahedral to strong axial lead to stabilization of an orbital singlet ground state. (B) Spin-orbit coupling in second order of this spin quintet $^5B_2$ ground state with ^5E removes the ground-state degeneracy, leading to zero field splitting with $D > 0$.

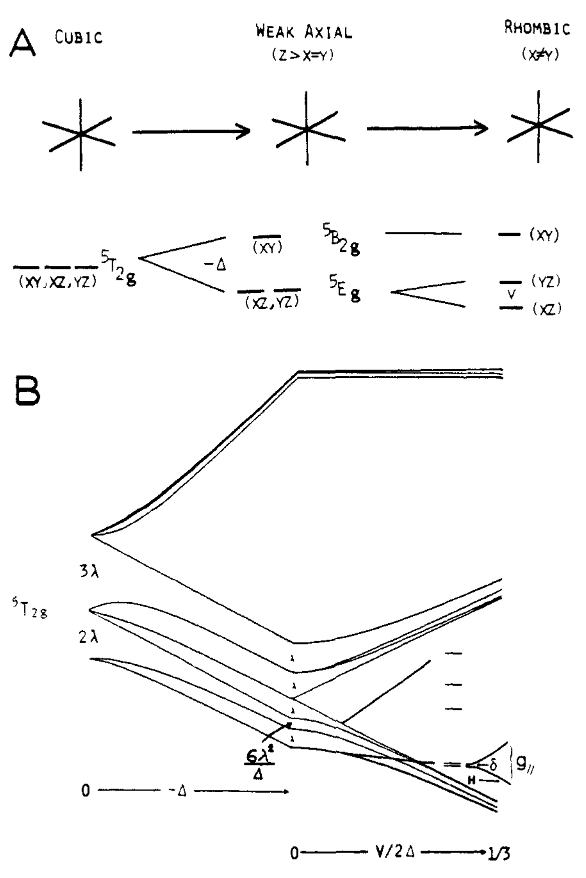

Figure 12. Ligand field theory for $^5T_{2g}$ ground state. (A) Under a weak axial distortion, an orbital doublet ground state is stabilized. (B) The effective $L' = -1$ orbital angular momentum leads to a complex multiplet splitting within $^5T_{2g}$ with an inverted Hund's rule ordering; the axial perturbation leaves orbital angular momentum in the ^5E component leading to a ladder of doublets unlike the splitting predicted by the spin Hamiltonian formalism. The insert shows the splitting of the lowest pair of sublevels in a magnetic field. A rhombic distortion leaves a non-Kramers doublet lowest; the splitting pattern converges with the predictions of the $S = 2$ spin Hamiltonian in the extreme rhombic limit, $V/2\Delta = {}^1/_3$.

of spin–orbit coupling (Figure 12A, middle) results in only partial quenching of the orbital angular momentum, and thus in-state spin–orbit splitting of the ^5E_g in D_{4h} or C_{4v} symmetry produces a manifold of five doublets each split by λ. Second-order spin–orbit coupling with the excited $^5B_2$ further splits the first excited doublet by $6\lambda^2/\Delta$. A rhombic perturbation is required to completely quench the orbital momentum; this perturbation leads to a rhombic zero field splitting δ within the lowest non-Kramers doublet of the ground state. (See expanded scale in Figure 11B.) It should be emphasized that the zero field splitting of the lowest levels of the ^5E_g have an energy pattern relating directly to λ which is quite different from that predicted by the spin Hamiltonian formalism, eq 1, except in the pure rhombic limit of $V/2\Delta = 1/3$ which corresponds to $E/D = 1/3$ in the spin Hamiltonian formalism.

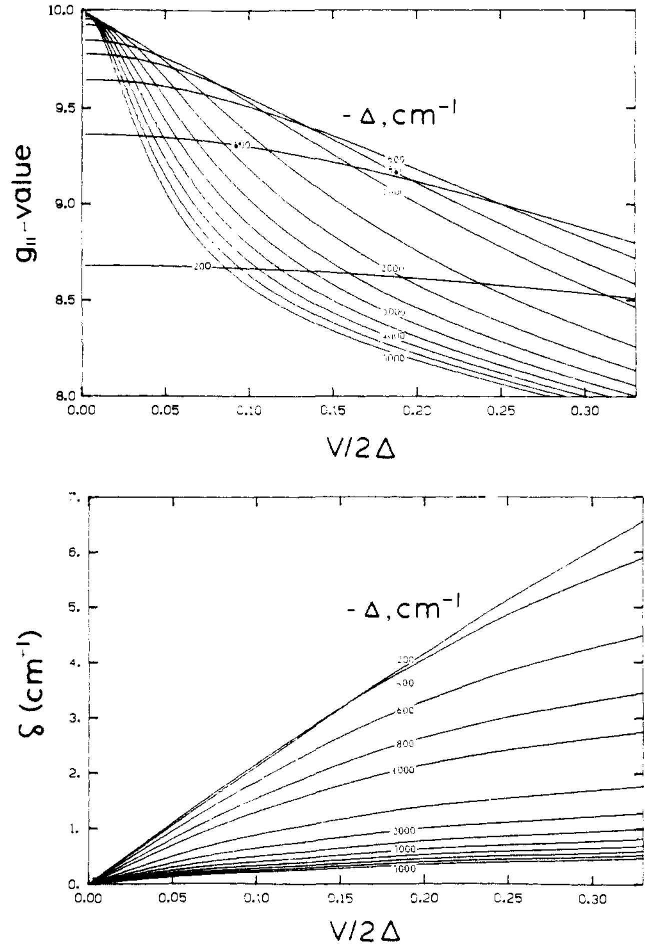

Figure 13. Ground-state parameters $g_\parallel$ (A) and rhombic splitting δ (B) for a $^5T_{2g}$ ground state as a function of axial (Δ) and rhombic (V) perturbations, calculated from the ligand field Hamiltonian (eq 7) for $\lambda = -80$ cm^{-1}.

Application of an external magnetic field in eq 8 allows calculation of the $g_\parallel$ value of the lowest doublet, and the variation of $g_\parallel$ and δ with the rhombicity $V/2\Delta$ is plotted in Figure 13 for a range of Δ values. It is clear that these parameters sensitively reflect the t_{2g} orbital splittings over a wide range of V and Δ; the variation of δ with axial orbital splitting (Δ) makes this parameter particularly sensitive to geometry. As the t_{2g} axial orbital splitting increases ($-\Delta$ increases), δ becomes small over the entire range of $V/2\Delta$ and thus small values of δ (<4 cm^{-1}) are expected for a large splitting of the d_{xy} relative to the $d_{xz,yz}$ orbitals which corresponds to a distortion toward a square-pyramidal limiting geometry. δ reaches a maximal value near the rhombic limit for nearly degenerate orbital ground state and is associated with roughly octahedral coordination ($\delta > 5$ cm^{-1}). For even moderate rhombic distortions ($V/2\Delta > 0.15$) the value of δ becomes nearly independent of V and reflects a narrow range of orbital splittings (Δ). The value of $g_\parallel$ within the lowest doublet also varies, decreasing from 10 at the axial limit ($V/2\Delta = 0$) through 8 at the extreme rhombic limit ($V/2\Delta = 1/3$),[56] but since the experimental value of $g_\parallel$ is less reliable than δ it is less useful in making structural

---

(56) The deviations of the effective g value from 8 in the rhombic limit of Figure 13 result from a significant orbital contribution to the Zeeman interaction which develops as the orbital splitting (Δ) approaches the magnitude of the spin–orbit coupling parameter λ.

correlations. Figure 13 illustrates the variation of the ground-state parameters with t_{2g} orbital splittings.

The experimental values of δ and $g_{\parallel}$ which have been obtained from analysis of MCD saturation data for the two proteins (FeSD and SBL) and the two model complexes ([Fe(TMC)Br]Br and $Fe(NH_4)_2(SO_4)_2{\cdot}6H_2O$) have been interpreted in terms of ferrous orbital splittings based on these calculations. The values of Δ and $V/2\Delta$ appropriate for the proteins and model complexes are given in Table I. Evaluation of δ and $g_{\parallel}$ in terms of either pure *xy* (eq 6) or mixed polarization (eq 7) for the MCD intensity leads to the conclusion that for each complex a ground orbital doublet is experimentally the correct limit for the ferrous complexes studied, emphasizing the generality of the weak axial distortion in these ferrous complexes. The small value of δ and large $g_{\parallel}$ observed for the C_{4v} model complex are consistent with a large axial t_{2g} splitting plus a small rhombic component. The plots in Figure 13 allow a quantitative estimate of the orbital splittings to be made, and for $\lambda = -100$ cm^{-1} the values $\Delta = -2000$ cm^{-1} with $V/2\Delta = 0.15$ have been obtained. (Note that since δ represents the most reliable parameter resulting from these analyses, Δ is fairly well defined, but the rhombicity $V/2\Delta$ is less sensitively determined.) The large value of δ observed for the ferrous Tutton salt, combined with a $g_{\parallel}$ value near 8.0, requires a small axial ($\Delta = 250$ cm^{-1}) and large rhombic t_{2g} splitting. This analysis can be extended to the two proteins, yielding (Table I) splittings similar to those found for the C_{4v} model (for FeSD), and for the octahedral model (for SBL). The results for FeSD indicate a larger rhombic distortion than present in the square pyramidal model complex consistent with a lowering of the electronic symmetry to at most C_{2v}.

The sensitivity of the ground-state parameters to structural perturbations allows them to be used to complement the excited-state d → d spectra as probes of ligand interactions at the ferrous site. In the data presented in Figure 4, both ground and excited state properties of the ferrous sites in FeSD and SBL are unchanged in the presence of high concentrations of N_3^-, which is known to bind to the ferric active sites in both of these proteins. The magnitude of the perturbation which will result from ligand substitution within a ferrous complex is calibrated within our study by a set of square pyramidal model complexes in which the apical ligand is systematically varied from Br^- to N_3^- to $NC{-}CH_3$. An electronic structural change is clearly observed in both the excited-state spectra, where a shift in the highest energy spin allowed d → d transition indicates an increase in the overall splitting within the d orbitals, and in the ground-state MCD data which is reflected in distinct saturation magnetization profiles. These experimental results indicate that small anions likely do not coordinate directly to the ferrous sites in the two proteins.

Susceptibility data are available for the two model complexes.[28,38] For the ferrous Tutton salt, an initial splitting of 6.5 cm^{-1} and an associated $g_{\parallel} = 10.4$ have been reported,[38b] which compare reasonably with the values of δ and $g_{\parallel}$ obtained in our analysis. The reported value of $g_{\parallel}$ is larger than ours but is likely an overestimate in that it exceeds the maximum value predicted by ligand field theory. For the C_{4v} model complex, an estimate of the zero field splitting parameter $D = 5.7$ cm^{-1} has been obtained from susceptibility data interpreted in terms of the spin Hamiltonian formalism,[28] assuming $D > 0$ in eq 1. Since this suggests a first sublevel splitting of 5.7 cm^{-1}, our data, which give this splitting accurately, disagree with the previous result. A number of considerations support our results on this complex. First, simple ligand field theory arguments lead to a prediction of $D < 0$ for the square-pyramidal geometry of this complex, contradicting the basic assumption of the earlier analysis. Further, Kennedy and Murray[57] have shown that there is a fundamental ambiguity in the sign of the zero field splitting parameter D obtained from the magnetic susceptibility of a powder (for example, see Figure 4 of ref 57). Finally, the conventional susceptibility methods involving application of a spin Hamiltonian for modeling the ground-state splittings are not valid in the limit of an orbitally degenerate or near-degenerate ground state which is usually the case for ferrous complexes, although this has not generally been recognized. In particular, as noted above, the splittings predicted from the spin Hamiltonian for $D < 0$ are not the same as the actual sublevel splittings (Figure 12). Note that in our analysis we use δ and to some extent $g_{\parallel}$ to get t_{2g} orbital splittings in ferrous complexes which have previously only occasionally been estimated on the basis of limited thermal population of the orbital levels detected in Mössbauer spectroscopy. It will clearly be important now to directly observe these orbital splittings to further evaluate the accuracy of this ligand field analysis of δ and $g_{\parallel}$.

Discussion

MCD studies of the ferrous complexes in two proteins and a number of model complexes have demonstrated the value of this technique in probing the electronic and geometric structures of ferrous active sites, which have often been regarded as spectroscopically inaccessible by absorption and EPR techniques. The key insight has been developed through an understanding of the temperature and field dependence of MCD arising from a ground non-Kramers doublet. These results indicate that the magnetic field induced mixing of wave functions within a rhombically split non-Kramers doublet is the origin of nesting behavior for saturation magnetization curves in these systems rather than thermal population over axial zero field split components.

An analysis of the ligand field origins of the ground-state splittings for ferrous iron shows that the dominant effect is from spin–orbit coupling within the low-symmetry split $^5T_{2g}$ state. These considerations indicate that the principal contribution to the spin Hamiltonian parameter D in ferrous complexes is from the axial splitting within the t_{2g} set of orbitals, D decreasing with increasing Δ. This sensitivity makes D particularly useful as a probe of π interactions in these complexes. However, this spin Hamiltonian parameter is meaningful only in the limit of a nondegenerate orbital ground state as is obtained under perturbations leading to t_{2g} splittings with $\Delta > 0$ or in the extreme rhombic limit of either splitting scheme. The range of validity is limited, however: when the ^5E component of the $^5T_2$ state is lowest (weak axial distortion), the ground state has orbital as well as spin degeneracy, and the entire ligand field Hamiltonian must be solved within the full $^5T_2$ basis (eq 8). Distorted octahedral and five-coordinate ferrous complexes generally have a weak axial perturbation and thus the splitting of their ground-state sublevels is very different from those predicted by an $S = 2$ spin Hamiltonian. The ligand field Hamiltonian for spin-orbit effects within the split t_{2g}, including Zeeman interactions, can be used to estimate t_{2g} orbital splittings from the rhombic splitting δ and the $g_{\parallel}$ for the ground doublet for ferrous complexes with nearly orbitally degenerate ground states (Figure 13). A general correlation can be made from ligand field theory that small orbital splittings (~250–500 cm^{-1}) with large rhombicity are indicative of near-octahedral electronic symmetry, while large axial splittings (~1200–2000 cm^{-1}) with smaller rhombicity reflect square-pyramidal electronic symmetry.

General trends are also evident in the experimental ligand field splittings of excited states relating to variation of geometry: roughly octahedral coordination is associated with an overall splitting of E and T_2 by approximately 10 000 cm^{-1}. A weak axial distortion removes the degeneracy of the excited orbital doublet and in the limit of square-pyramidal five-coordination the splitting between the highest two states is nearly 5000 cm^{-1}. Experimentally, the overall d-orbital splitting in five-coordinate complexes is greater in the square-pyramidal than in the trigonal-bipyramidal limit. In the four-coordinate T_d site the ligand field is reduced ($Dq_{T_d} \sim {}^4/_9 Dq_{O_h}$); however, flattening to a square-planar structure leads to large ligand field splittings and with interconfiguration interaction (4s mixing) to a $^5A_1$ (d_{z^2}) ground state. These general trends provide a basis for making geometric structure predictions from splittings observed in ligand field ground and excited state spectra in ferrous complexes.

The biochemical relevance of these studies first of all relates to the development of an effective probe of ferrous sites and their interactions in non-heme Fe metalloenzymes. The characteristic

---

[57] Kennedy, B. J.; Murray, K. S. *Inorg. Chem.* **1985**, *24*, 1557–1560.

excited-state spectra and excited-state splittings observed for five versus six coordination provide information on the coordination number of the ferrous complex. Differences in the spectra observed for FeSD and SBL indicate distinct structures for these ferrous active sites, FeSD being five coordinate square pyramidal and SBL being distorted octahedral. These spectra also contain detailed geometric structural information relating to effective symmetry at the ferrous site, which defines a limiting electronic symmetry of ligand field interactions. This may be distinct from the geometric information obtained from crystallographic studies, but it relates more directly to the chemistry of the metal center in its electronic structural origins. These comments are especially pertinent to the data for FeSD, for which crystallographic structures are emerging.[7-9] The electron density map for ferric SD at 3 Å resolution has been interpreted in terms of five coordination at iron, and no significant change is detected at this resolution in a difference density map for the ferrous derivative.[9] The results of our MCD studies, which require five coordination for the ferrous site, are consistent with the crystallographic data, indicating that the coordination number of the iron does not change on reduction. This contrasts with the decrease in coordination number observed for the active site of Cu-Zn SD on reduction,[53] relating to loss of a histidine imidazole ligand. Refinement of the crystal structure for ferric SD has led to a prediction of trigonal-bipyramidal geometry for the iron;[9] however, the actual site symmetry is expected to be lower and in fact the MCD spectroscopic data are consistent with an effective symmetry for the iron which is closer to a square-pyramidal electronic symmetry with $d_{xz,yz}$ containing the extra electron involved in electron transfer to O_2^-.

The sensitivity of the ligand field excited state spectra and the ground state properties on the environment of the iron makes temperature-dependent MCD particularly powerful as a probe of changes in structure associated with ligand binding. the apparent absence of ligand binding in the ferrous derivatives of FeSD and SBL has important mechanistic implications, suggesting that the redox reactivity of these sites involves outer-sphere electron transfer rather than an inner-sphere mechanism. Kinetic analysis by Fee et al. of superoxide dismutation by FeSD has already suggested that anions do not bind to the ferrous site;[11,17,18] the direct probe of ligand binding afforded by the spectroscopic approaches reported here is consistent with an outer-sphere mechanism for FeSD in its reducing cycle. This outer-sphere redox chemistry, while different from the proposed mechanism for Cu-Zn SD, would be consistent with protecting the site from Fenton-type chemistry[54,55] by peroxide reaction with Fe^{2+} as well as inhibition by the peroxide-Fe^{3+} product complex.

A comparison of the results for FeSD and SBL emphasizes that, while both suggest outer-sphere reactivity, a key distinction must be made between the ferrous derivatives of the two resting enzymes. Both of these active sites appear to interact with dioxygen species in the ferrous oxidation state. However, ferrous SBL is stable toward the reaction with O_2 leading to autoxidation; this difference in O_2 reactivity appears to relate to the increased coordination number for this ferrous site relative to SD, apparently relating to an increase in the number of imidazole ligands stabilizing Fe^{2+}. Further, for SBL the active ferrous species is associated with bound substrate radical which appears to be formed during turnover by substrate oxidation. Thus, the anaerobic substrate active site complex, rather than the resting enzyme, is thus the species most closely related to the structure of the ferrous site involved in the enzyme mechanism. Parallel absorption, CD, and variable-temperature, variable-field MCD experiments probing substrate and analogue interactions with ferrous sites in several mononuclear non-heme iron enzymes are in progress.

Acknowledgment. This work is supported by the National Institutes of Health (Grant GM40392). J.W.W. thanks the NIH for a postdoctoral fellowship (Grant AMO7456).

Guyanin, a Novel Tetranortriterpenoid: Structural Characterization by 2D NMR Spectroscopy and X-ray Crystallography

Stewart McLean,*[†] Marion Perpick-Dumont,[†] William F. Reynolds,*[†] Jeffery F. Sawyer,[†] Helen Jacobs,[‡] and Frank Ramdayal[‡]

Contribution from the Department of Chemistry, University of Toronto, Toronto, Ontario, Canada M5S 1A1, and Centre for Natural Products Chemistry, University of Guyana, Georgetown, Guyana. *Received September 14, 1987*

Abstract: The skeletal structure of guyanin, a tetranortriterpene of an unprecedented structural type, has been unambiguously deduced by using $^{13}C-^{1}H$ shift-correlated spectra with delay times optimized for polarization transfer via two-bond and three-bond $^{13}C-^{1}H$ coupling. Spectra were obtained by using a modified version of our XCORFE pulse sequence. X-ray crystallography was used to confirm the structure and establish the stereochemistry of guyanin. The conformation in solution is the same as in the solid state, with $^{1}H-^{1}H$ coupling constants, NOE data, and ^{13}C T_1 relaxation times all suggesting that the molecule has little conformational mobility. Possible biogenetic origins of this unique molecule are discussed.

There has been intense interest in the application of two-dimensional (2D) NMR techniques to the elucidation of structures of complex organic molecules.[1] These techniques correlate a variety of combinations of ^{1}H and ^{13}C spectral properties by the application of specialized pulse sequences. The scope, value, and limitations of each technique in structural elucidation depend upon the type of data correlated, the dependability of the correlations (i.e., the degree of suppression of spurious correlations), and the sensitivity of the experiment. In most cases, the utility of a particular new technique has been illustrated by a detailed

---

[†] University of Toronto.

[‡] University of Guyana.

[1] Morris, G. A. *Magn. Reson. Chem.* **1986**, *24*, 371.

0002-7863/88/1510-5339$01.50/0